This article has been accepted for publication in a future issue of this journal, but has not been fully edited. Content may change prior to final publication. Citation information: DOI 10.1109/JESTPE.2021.3135380, IEEE Journal of Emerging and Selected Topics in Power Electronics

Integrated Optimization of Dual-Active-Bridge DC-DC Converter with ZVS for Battery Charging Applications

Li Jiang, *Graduate Student Member*, *IEEE*, Yao Sun, *Member*, *IEEE*, Yong Li, *Senior Member*, *IEEE*, Zhongting Tang, *Member*, *IEEE*, Fulin Liu, Yongheng Yang, *Senior Member*, *IEEE*, Mei Su and Yijia Cao, *Senior Member*, *IEEE*

Abstract—In this paper, the dual-active-bridge (DAB) DC-DC converter with phase-shift control is explored extensively, and the optimal performances obtained with different objectives are comparatively analysis in each mode. Firstly, the principle and operating modes of the TPS control are introduced in detail. Secondly, the electrical characteristics of the converter in each operating mode are systematically derived. Thirdly, the resonant commutation in each dead-band is analyzed and the soft-switching areas of the converter are obtained. Then, based on the zero-voltage-switching (ZVS), the peak and root mean square (RMS) of the inductor current, backflow power and operating losses are taken as the optimization objectives, and the obtained optimized results are contrastively analyzed. The commonalities of the optimization results with different objectives in modes I, II, and III are revealed, and the differences of optimization characteristic in mode IV are present, as a guidance for practice design and operation. Experiments are performed to demonstrate the theoretical analysis.

***Index Terms*—Dual-active-bridge (DAB), inductor current, ZVS, triple-phase-shift (TPS), backflow power, losses.**

I. INTRODUCTION

DUAL-active-bridge (DAB) DC-DC converters, as shown in Fig. 1, have received extensive attention. Because of its high power density, high voltage level, zero voltage switching (ZVS), electrical isolation, bidirectional energy transmission, and symmetrical structure, DAB converters have been increasing employed in various applications [1], [2], e.g., in renewable energy systems [3], electric vehicles [4], solid-state transformers [5], [6], battery energy storage systems [7].

The modulations of the DAB converter mainly adopt the phase-shift-control (PSC) [1], which is also the basis of the optimization analysis [8]. Single-phase-shift (SPS) control is considered to be the simplest modulation strategy. It only adjusts the phase-shift-angle (PSA) between the H-bridges, and does not have the internal PSA in each bridge [9], [10]. Due to the lack of control freedom, it is difficult to improve the performance of the converter, therefore, it is not well accepted [11]. For the dual-phase-shift (DPS) control, the H-bridges have the same internal PSA, and the external PSA between them can also be adjusted [12], [13]. However, only two PSAs can be regulated, and the same internal PSAs limit the flexibility of converter control. In addition, unlike the DPS, only one H-bridge has an internal PSA in the extended-phase-shift (EPS) control, and the AC side of the other H-bridge is still a square wave, which also has two control degrees of freedom [5], [14]. To improve the operating performance, triple-phase-shift (TPS) control is proposed [15]. There are an external PSA and two internal PSAs that can be different [16]. The TPS control has three control variables, which further increases the control flexibility [17].

Although the converter modulation strategies based on PSC are diverse, other modulation strategies can all be regarded as special cases of TPS control [1], [18]. Thus, converter analysis based on TPS control is universal.

Since the modulation strategy based on PSC is adopted, as the control variables, the optimization of the PSAs in the feasible region is necessary for the predetermined optimization objective. Thus, it is important to study the optimized operation of DAB converters. The constraints that need to be considered in the optimization depend on various aspects, e.g., the operation modes, ZVS, and control objectives, and so on.

In addition, the selection of the objectives for the optimal operation of the DAB converter is diverse. The root mean square (RMS) of the inductor current is the main reason for the ohmic losses, such as line loss, and iron loss of the magnetic devices. Taking it as the optimization objective, reference [11] analyzes the characteristics of the converter's optimized operation under SPS, EPS and TPS control, respectively. Reference [16] introduces an model to describe the analytic expressions of the DAB converter under TPS control, and the

This work was supported in part by the Key Research and Development Program of Hunan Province of China under Grant 2018GK2031, in part by the independent research project of State Key Laboratory of Advance Design and Manufacturing for Vehicle Body under Grant 71965005, in part by the national Natural Science Foundation of China (NSFC) under Grant 51822702, in part by the 111 Project of China under Grant B17016, and in part by the Excellent Innovation Youth Program of Changsha of China under Grant KQ1802029. *(Corresponding author: Yao Sun, Yong Li.)*

L. Jiang, Y. Li, and Y. Cao are with the College of Electrical and Information Engineering and State Key Laboratory of Advance Design and Manufacturing for Vehicle Body, Hunan University, Changsha 410082, China (e-mail: jiangli0924@hnu.edu.cn, yongli@hnu.edu.cn, yjcao@hnu.edu.cn).

Y. Sun, F. Liu and M. Su are with the School of Automation, Central South University, Changsha 410083, China (e-mail: yaosun@csu.edu.cn, bxliufulin@gmail.com, sumeicsu@mail.csu.edu.cn).

Z. Tang is with Department of Energy Technology Aalborg University, Aalborg 9220, Denmark (e-mail: zta@et.aau.dk).

Y. Yang is with the College of Electrical Engineering, Zhejiang University, Hangzhou 310007, China (e-mail: yang_yh@zju.edu.cn).

This article has been accepted for publication in a future issue of this journal, but has not been fully edited. Content may change prior to final publication. Citation information: DOI 10.1109/JESTPE.2021.3135380, IEEE Journal of Emerging and Selected Topics in Power Electronics

optimal modulation scheme with minimum RMS of the inductor current is derived. Similarly, the minimization of the RMS current also necessary for three-phase applications [19]. Moreover, the peak current minimization is beneficial to reduce current stress of the current, and can also reduce the magnetic flux variation of magnetic devices, prevent magnetic flux saturation and reduce hysteresis losses [20]. Reference [21] proposes a general analysis method for DAB converters using TPS control, and derives the control rules that meets the required power transmission with the minimum current stress.

The reverse flow of energy is one of the disadvantages of DAB converters, which is also defined as backflow power [5]. Backflow power does not contribute to the power transmission, which is essentially caused by the reactive current [22]. The larger the backflow power, the larger the RMS of the current, and the lower the converter efficiency. Therefore, its minimization is also necessary. Reference [23] establishes a mathematical model of the DAB converter with a three-level modulation by a harmonic analysis method, and proposes a method for minimizing backflow power. Here, the modulation strategy is similar to TPS control. Global optimal PSAs that minimize the backflow power under four different operating scenarios are presented in [24], and the efficiency improvement of the proposed method is verified. In order to improve the operating efficiency, it is necessary to analyze and optimize the losses of the converter. An optimal modulation scheme that enables minimum conduction and copper losses of DAB converter an automotive application is presented in [25]. Reference [26] analyzes the switching characteristic of DAB converter under DPS control, establishes a power loss model to predict the dissipated power for each component. Further, the efficiency-optimized characteristic is presented.

Considering the diversity of PSCs and optimization objectives, there are abundant researches on different optimization objectives under different modulation strategies. However, the operating performances of the converters obtained by different optimization strategies have not been compared, and an integrated study is necessary. The TPS control is adopted in the paper, which covers all other phase-shift modulations. Moreover, the different optimization objectives are considered for comparative analysis. As a synthesis analysis of modulation and optimization of DAB converter, the rest of paper is organized as follows. In Section II, the TPS control and operating modes of the converter are analyzed. The soft switching regions are derived in Section III. In Section IV, the loss model of the converter is established. In Section V, the optimization performances obtained by different objectives are comparatively analyzed. Section VI is the experimental verification and Section VII is the conclusion.

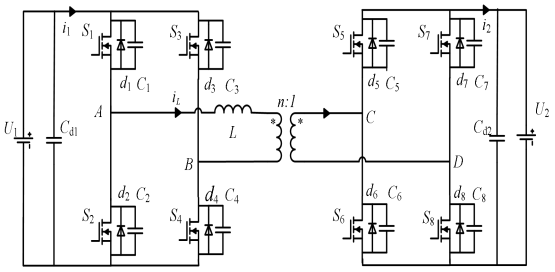

Fig. 1. Schematic of a DAB converter.

II. TPS Control and Operation Mode Analysis

As shown in Fig. 1, the input voltage is U_1, the output voltage is U_2, and the transformer turn-ratio is n : 1. Define T_{hs} as a half of a switching cycle, the voltages on the AC side of the primary and secondary H-bridge are V_{AB} and V_{CD} respectively, and V'_{CD} is the primary equivalent voltage of V_{CD}. In a half cycle, the ratio of the time corresponding to the high level of V_{AB} (V_{CD}) to T_{hs} is defined as the duty ratio D_1 (D_2). The ratio of the phase difference between V_{AB} and V_{CD} to π is defined as D_3, and the ratio of the dead-band to T_{hs} is defined as DT. The energy from U_1 to U_2 is defined as forwarding transmission, i.e., $D_3 \geq 0$. Define the voltage ratio $k = nU_2 / U_1$. When $k \leq 1$, to achieve the ZVS operation, the duty cycle of the high-voltage side is generally less than that of the low-voltage side, that is, $D_1 \leq D_2$. Only the forward energy transmission when $k \leq 1$ is analyzed.

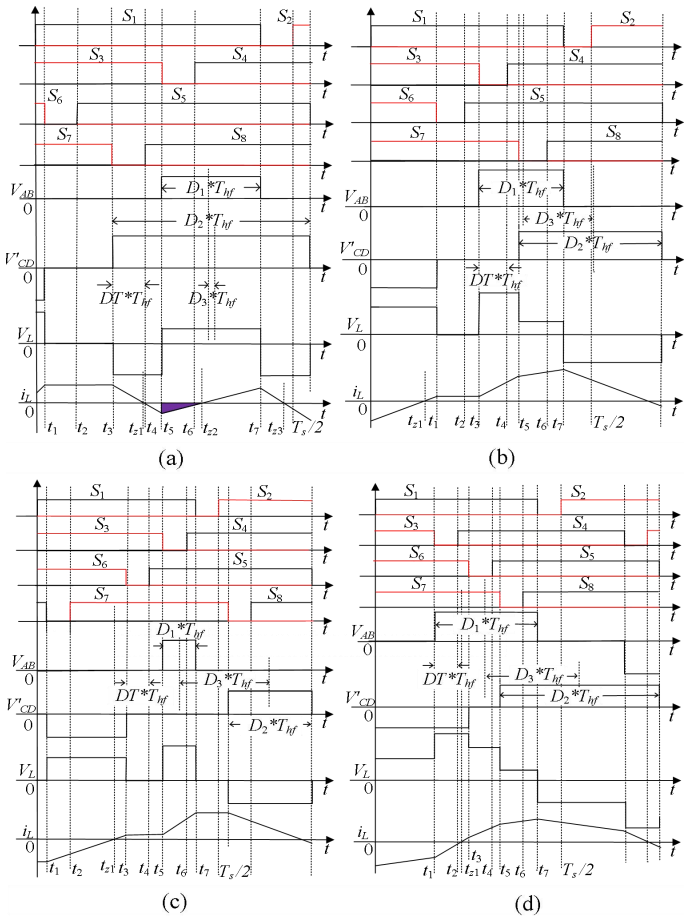

Fig. 2. Steady state waveforms of the DAB converter with the TPS control. (a) Mode I. (b) Mode II. (c) Mode III. (d) Mode IV.

Depending on the (D_1, D_2, D_3), there are six operation modes [1]. When $0 \leq D_3 \leq 0.5$ and $0.5 \leq D_3 \leq 1$, the transmission powers are the same, and the operating characteristics will be deteriorated significantly if $0.5 \leq D_3 \leq 1$ [1]. Therefore, only the operation modes of $0 \leq D_3 \leq 0.5$ are analyzed. The steady state waveforms of modes I, II, III, and IV are shown in Figs. 2(a), (b), (c), and (d), respectively. Mode I is defined as the rising edge of V_{AB} from 0 to U_1 lags the rising edge of V'_{CD} from 0 to nU_2. Mode II is defined as the rising edge of V_{AB} from 0 to U_1 lags the rising edge of V'_{CD} from $-nU_2$ to 0, but it is ahead of the

rising edge of V'_{CD} from 0 to nU_2, and the rising edge of V'_{CD} from 0 to nU_2 lags the falling edge of V_{AB} from U_1 to 0. Mode III is defined as the rising edge of V_{AB} from 0 to U_1 lags the rising edge of V'_{CD} from $-nU_2$ to 0, and the rising edge of V'_{CD} from 0 to nU_2 lags the falling edge of V_{AB} from U_1 to 0. Mode IV is defined as the rising edge of V'_{CD} from $-nU_2$ to 0 and the rising edge from 0 to nU_2 lag the rising edge of V_{AB} from 0 to U_1, but they lead the falling edge of V_{AB} from U_1 to 0.

The operating conditions of each mode are constrained as

1) Operation mode I:

$$-D_1 + D_2 - 2D_3 \geq 0 \tag{1}$$

2) Operation mode II:

$$\begin{cases} -D_1 + D_2 - 2D_3 \leq 0 \\ D_1 + D_2 + 2D_3 - 2 \leq 0 \\ -D_1 - D_2 + 2D_3 \leq 0 \end{cases} \tag{2}$$

3) Operation mode III:

$$\begin{cases} D_1 + D_2 - 2D_3 \leq 0 \\ D_1 + D_2 + 2D_3 - 2 \leq 0 \end{cases} \tag{3}$$

4) Operation mode IV:

$$\begin{cases} -D_1 - D_2 + 2D_3 \leq 0 \\ -D_1 - D_2 - 2D_3 + 2 \leq 0 \end{cases} \tag{4}$$

To simplify the analysis, the effect of the dead-band is ignored. Taking the mode I as an example, as shown in Fig. 2(a), in the first half cycle of [0, T_s /2], the converter has eight switching states. According to the operating waveforms of the converter at steady state, the inductor current is anti-symmetrical in each half-cycle, that is, $i_L(0) = -i_L(T_s/2)$. Therefore, the current of the inductor L at mode I can be expressed as in (5), and t_1-t_7 are listed in Table I.

$$i_L(t) = \begin{cases} \dfrac{kU_1}{L}t + \dfrac{U_1}{4Lf_s}\begin{bmatrix}(k-1)D_1 \\ -2kD_3 + 2kDT\end{bmatrix} & (0 \leq t \leq t_1) \\ \dfrac{U_1}{4Lf_s}(-D_1 + kD_2) & (t_1 \leq t \leq t_3) \\ -\dfrac{kU_1}{L}t + \dfrac{U_1}{4Lf_s}\begin{bmatrix}2k-(k+1)D_1 \\ +2kD_3 - 2kDT\end{bmatrix} & (t_3 \leq t \leq t_5) \\ \dfrac{(1-k)U_1}{L}t + \dfrac{U_1}{4Lf_s}\begin{bmatrix}2k-2+ \\ (1-k)D_1 \\ +2kD_3 \\ +(2-2k)DT\end{bmatrix} & (t_5 \leq t \leq t_7) \\ -\dfrac{kU_1}{L}t + \dfrac{U_1}{4Lf_s}\begin{bmatrix}2k+(1-k)D_1 \\ +2kD_3 - 2kDT\end{bmatrix} & (t_7 \leq t \leq \dfrac{T_s}{2}) \end{cases} \tag{5}$$

where f_s is the switching frequency.

According to Fig. 2(a) and Table I, the power reference is defined as P_{base}, and the normalized transmission power in mode I can be derived as

$$\overline{P} = \frac{P}{P_{base}} = \frac{U_1 \dfrac{1}{T_s/2}\int_{t_5}^{t_7} i_L(t)\,dt}{U_1^2/8Lf_s} = 4kD_1D_3 \tag{6}$$

where P is the power. The maximum current is obtained at $t = t_7$, defined as i_p, and the current reference is defined as i_{base}. The normalized peak current $\overline{i_p}$ is expressed as

$$\overline{i_p} = \frac{i_L(t_7)}{i_{base}} = \frac{i_L(t_7)}{U_1/8Lf_s} = 2\begin{bmatrix}(1-k)D_1 + 2kD_3 \\ +(1-k)DT\end{bmatrix} \tag{7}$$

The inductor current crosses the horizontal axis at time $t = t_{z2}$. Based on (5), t_{z2} is derived as

$$t_{z2} = \frac{1}{4(k-1)f_s}\begin{bmatrix}2k-2+(1-k)D_1 \\ +2kD_3 + (2-2k)DT\end{bmatrix} \tag{8}$$

For DAB converter, the backflow power is defined as the part of the power returned to the input source in each switching cycle. As shown the shaded area in Fig. 2(a), it represents the integral of the feedback current on the time axis, which can reflect the magnitude of backflow power. The normalized backflow power is defined as

$$\overline{Q} = \frac{\dfrac{-U_1}{T_s/2}\int_{t_5}^{t_{z2}} i_L(t)dt}{P_{base}} = \frac{\left[(k-1)D_1 + 2kD_3\right]^2}{2(1-k)} \tag{9}$$

For mode I, the backflow power cannot be reduced to zero, because a certain backflow power is a prerequisite for the ZVS operation of S_3 and S_4. The normalized RMS of the inductor current is expressed as

$$\overline{i_{Lrms}} = \sqrt{\frac{\int_0^{T_s/2} i_L^2(t)\,dt}{i_{base}^2\, T_s/2}} = \frac{2\sqrt{3}}{3}\begin{bmatrix}(k-2)D_1^3 + 3D_1^2 + 3kD_1D_2^2 \\ -6kD_1D_2 + 12kD_1D_3^2 \\ -2k^2D_2^3 + 3k^2D_2^2\end{bmatrix}^{1/2} \tag{10}$$

Similarly, the analysis of modes II, III, and IV is gives as follows, and all time intervals are also listed in Table I. According to the analysis, for modes II and III, the converter operates without backflow power.

1) Operation mode II:

$$i_L(t) = \begin{cases} \dfrac{kU_1}{L}t + \dfrac{U_1}{4Lf_s}\begin{bmatrix}(k-1)D_1 \\ -2kD_3 + 2kDT\end{bmatrix} & (0 \leq t \leq t_1) \\ \dfrac{U_1}{4Lf_s}(-D_1 + kD_2) & (t_1 \leq t \leq t_3) \\ \dfrac{U_1}{L}t + \dfrac{U_1}{4Lf_s}\left[D_1 + kD_2 + 2DT - 2\right] & (t_3 \leq t \leq t_5) \\ \dfrac{(1-k)U_1}{L}t + \dfrac{U_1}{4Lf_s}\begin{bmatrix}2k-2+2kD_3 \\ +(1-k)D_1 \\ +(2-2k)DT\end{bmatrix} & (t_5 \leq t \leq t_7) \\ -\dfrac{kU_1}{L}t + \dfrac{U_1}{4Lf_s}\begin{bmatrix}2k+(1-k)D_1 \\ +2kD_3 - 2kDT\end{bmatrix} & (t_7 \leq t \leq \dfrac{T_s}{2}) \end{cases} \tag{11}$$

This article has been accepted for publication in a future issue of this journal, but has not been fully edited. Content may change prior to final publication. Citation information: DOI 10.1109/JESTPE.2021.3135380, IEEE Journal of Emerging and Selected Topics in Power Electronics

$$\begin{cases} \overline{P}=\dfrac{k}{2}\left[-\left(D_1-D_2\right)^2+4D_3\left(D_1+D_2-D_3\right)\right] \\ \overline{i_p}=2\left[\left(1-k\right)D_1+2kD_3\right] \\ \overline{i_{Lrms}}=\dfrac{\sqrt{6}}{3}\begin{bmatrix}\left(k-4\right)D_1^3+\left(3kD_2-6kD_3+6\right)D_1^2\\+\left(3kD_2+12kD_3-12k\right)D_1D_2\\+12kD_1D_3^2-\left(4k^2-k\right)D_2^3\\-\left(6kD_3-6k^2\right)D_2^2+12kD_2D_3^2-8kD_3^3\end{bmatrix}^{1/2} \end{cases} \tag{12}$$

TABLE I
TIME POINTS OF EACH OPERATION MODE

Time	Mode I	Mode II	Mode III	Mode IV
t_1	$\frac{T_s}{2}\left(\begin{matrix}-\frac{D_1}{2}+\frac{D_2}{2}\\+D_3-DT\end{matrix}\right)$	$\frac{T_s}{2}\left(\begin{matrix}-\frac{D_1}{2}+\frac{D_2}{2}\\+D_3-DT\end{matrix}\right)$	$\frac{T_s}{2}\left(\begin{matrix}-\frac{D_1}{2}-\frac{D_2}{2}\\+D_3-DT\end{matrix}\right)$	$\frac{T_s}{2}\left(\begin{matrix}1-D_1\\-DT\end{matrix}\right)$
t_2	$\frac{T_s}{2}\left(\begin{matrix}-\frac{D_1}{2}+\frac{D_2}{2}\\+D_3\end{matrix}\right)$	$\frac{T_s}{2}\left(\begin{matrix}-\frac{D_1}{2}+\frac{D_2}{2}\\+D_3\end{matrix}\right)$	$\frac{T_s}{2}\left(\begin{matrix}-\frac{D_1}{2}-\frac{D_2}{2}\\+D_3\end{matrix}\right)$	$\frac{T_s}{2}(1-D_1)$
t_3	$\frac{T_s}{2}\left(\begin{matrix}1-\frac{D_1}{2}-\frac{D_2}{2}\\+D_3-DT\end{matrix}\right)$	$\frac{T_s}{2}\left(\begin{matrix}1-D_1\\-DT\end{matrix}\right)$	$\frac{T_s}{2}\left(\begin{matrix}-\frac{D_1}{2}+\frac{D_2}{2}\\+D_3-DT\end{matrix}\right)$	$\frac{T_s}{2}\left(\begin{matrix}-\frac{D_1}{2}+\frac{D_2}{2}\\+D_3-DT\end{matrix}\right)$
t_4	$\frac{T_s}{2}\left(\begin{matrix}-\frac{D_1}{2}+\frac{D_2}{2}\\+D_3\end{matrix}\right)$	$\frac{T_s}{2}(1-D_1)$	$\frac{T_s}{2}\left(\begin{matrix}-\frac{D_1}{2}+\frac{D_2}{2}\\+D_3\end{matrix}\right)$	$\frac{T_s}{2}\left(\begin{matrix}-\frac{D_1}{2}+\frac{D_2}{2}\\+D_3\end{matrix}\right)$
t_5	$\frac{T_s}{2}\left(\begin{matrix}1-D_1\\-DT\end{matrix}\right)$	$\frac{T_s}{2}\left(\begin{matrix}1-\frac{D_1}{2}-\frac{D_2}{2}\\+D_3-DT\end{matrix}\right)$	$\frac{T_s}{2}\left(\begin{matrix}1-D_1\\-DT\end{matrix}\right)$	$\frac{T_s}{2}\left(\begin{matrix}1-\frac{D_1}{2}-\frac{D_2}{2}\\+D_3-DT\end{matrix}\right)$
t_6	$\frac{T_s}{2}(1-D_1)$	$\frac{T_s}{2}\left(\begin{matrix}-\frac{D_1}{2}+\frac{D_2}{2}\\+D_3\end{matrix}\right)$	$\frac{T_s}{2}(1-D_1)$	$\frac{T_s}{2}\left(\begin{matrix}1-\frac{D_1}{2}+\frac{D_2}{2}\\+D_3\end{matrix}\right)$
t_7	$\frac{T_s}{2}(1-DT)$	$\frac{T_s}{2}(1-DT)$	$\frac{T_s}{2}(1-DT)$	$\frac{T_s}{2}(1-DT)$

2) Operation mode III:

$$i_L(t)=\begin{cases} \dfrac{U_1}{4Lf_s}\left(-D_1-kD_2\right) & (0\le t\le t_1) \\ \dfrac{kU_1}{L}t+\dfrac{U_1}{4Lf_s}\begin{bmatrix}\left(k-1\right)D_1\\-2kD_3+2kDT\end{bmatrix} & (t_1\le t\le t_3) \\ \dfrac{U_1}{4Lf_s}\left(-D_1+kD_2\right) & (t_3\le t\le t_5) \\ \dfrac{U_1}{L}t+\dfrac{U_1}{4Lf_s}\begin{bmatrix}D_1+kD_2\\+2DT-2\end{bmatrix} & (t_5\le t\le t_7) \\ \dfrac{U_1}{4Lf_s}\left[D_1+kD_2\right] & (t_7\le t\le \dfrac{T_s}{2}) \end{cases} \tag{13}$$

$$\begin{cases} \overline{P}=2kD_1D_2 \\ \overline{i_p}=2\left(D_1+kD_2\right) \\ \overline{i_{Lrms}}=\dfrac{2\sqrt{3}}{3}\begin{bmatrix}-2D_1^3+3D_1^2-2k^2D_2^3\\+3k^2D_2^2-6kD_1D_2\\+12kD_1D_2D_3\end{bmatrix}^{1/2} \end{cases} \tag{14}$$

3) Operation mode IV:

$$i_L(t)=\begin{cases} \dfrac{kU_1}{L}t+\dfrac{U_1}{4Lf_s}\begin{bmatrix}\left(k-1\right)D_1\\-2kD_3+2kDT\end{bmatrix} & (0\le t\le t_1) \\ \dfrac{\left(1+k\right)U_1}{L}t+\dfrac{U_1}{4Lf_s}\begin{bmatrix}\left(k+1\right)D_1-2kD_3\\+\left(2+2k\right)DT-2\end{bmatrix} & (t_1\le t\le t_3) \\ \dfrac{U_1}{L}t+\dfrac{U_1}{4Lf_s}\left[D_1+kD_2+2DT-2\right] & (t_3\le t\le t_5) \\ \dfrac{(1-k)U_1}{L}t+\dfrac{U_1}{4Lf_s}\begin{bmatrix}2k-2+\left(1-k\right)D_1\\+2kD_3\\+\left(2-2k\right)DT\end{bmatrix} & (t_5\le t\le t_7) \\ -\dfrac{kU_1}{L}t+\dfrac{U_1}{4Lf_s}\begin{bmatrix}2k+\left(1-k\right)D_1\\+2kD_3-2kDT\end{bmatrix} & (t_7\le t\le \dfrac{T_s}{2}) \end{cases} \tag{15}$$

$$\begin{cases} \overline{P}=k\begin{bmatrix}-\left(D_1^2+D_2^2\right)+2\left(D_1+D_2\right)\\-\left(2D_3-1\right)^2-1\end{bmatrix} \\ \overline{i_p}=2\left[\left(1-k\right)D_1+2kD_3\right] \\ \overline{Q}=\dfrac{1}{2\left(k+1\right)}\left[\left(k+1\right)D_1+2kD_3-2k\right]^2 \\ \overline{i_{Lrms}}=\dfrac{2\sqrt{3}}{3}\begin{bmatrix}-2D_1^3-\left(6kD_3-3k-3\right)D_1^2\\+12kD_1D_3-6k\left(D_1+D_2\right)\\-2k^2D_2^3-\left(6kD_3-3k^2-3k\right)D_2^2\\+12kD_2D_3-8kD_3^3+12kD_3^2\\-12kD_3+4k\end{bmatrix}^{1/2} \end{cases} \tag{16}$$

III. ANALYSIS OF ZVS CONSTRAINTS

For the DAB converter, the premise for the switches to turn on with ZVS is that their anti-parallel diodes are turned on. Due to the symmetry, only half of the switching cycle is analyzed. Taking the mode I as an example, the resonant commutations in the dead-band are analyzed firstly in this section [15]. The corresponding circuits are shown in Fig. 3.

During [t_1, t_2], as shown in Fig. 2(a), which is a dead-band, S_1, S_3, and S_7 are on, S_6 is turned off at t_1. The inductor L resonates with C_5 and C_6 to complete the process of discharging C_5 and charging C_6, and the equivalent circuit is shown in Fig. 3(a). Since $i_L(t)\ge 0$, the clamping effect disappears after C_5 is discharged, then d_5 is turned on, so that S_5 can be turned on at t_2 with ZVS. The voltage of C_5 is derived as

$$u_{C5}(t-t_1)=U_{m5}\sin\left(\omega_5(t-t_1)-\alpha_5\right) \tag{17}$$

where $\omega_5=n/\sqrt{L(C_5+C_6)}$, $U_{m5}=\sqrt{Z_5^2i_L(t_1)^2+U_2^2}$, $Z_5=\sqrt{L/(C_5+C_6)}$, $\tan\alpha_5=U_2/(Z_5 i_L(t_1))$.

Similarly, according to Figs. 3(b), (c), and (d), the voltages of parasitic equivalent output capacitors in [t_3, t_4], [t_5, t_6], and [t_7, $T_s/2$] are also expressed in (18).

This article has been accepted for publication in a future issue of this journal, but has not been fully edited. Content may change prior to final publication. Citation information: DOI 10.1109/JESTPE.2021.3135380, IEEE Journal of Emerging and Selected Topics in Power Electronics

$$\begin{cases} u_{C5}(t-t_1)=U_{m5}\sin\left(\omega_5(t-t_1)-\alpha_5\right) \\ u_{C8}(t-t_3)=U_{m8}\sin\omega_8\left(t-t_3\right)-U_2 \\ u_{C4}(t-t_5)=-U_{m4}\sin\left(\omega_4\left(t-t_5\right)+\alpha_4\right)+nU_2-U_1 \\ u_{C2}(t\text{-}t_7)=U_{m2}\sin\left(\omega_2\left(t\text{-}t_7\right)+\alpha_2\right)-nU_2 \end{cases} \tag{18}$$

where $\tan\alpha_5=U_2/(Z_5 i_L(t_1))$, $\omega_8=n/\sqrt{L(C_7+C_8)}$, $U_{m8}=Z_8 i_L(t_3)$, $Z_8=\sqrt{L/(C_7+C_8)}$, $\omega_4=1/\sqrt{L(C_3+C_4)}$, $U_{m4}=\sqrt{Z_4 i_L(t_5)^2+(nU_2)^2}$, $\tan\alpha_4=nU_2/(Z_4 i_L(t_5))$, $Z_4=\sqrt{L/(C_3+C_4)}$, $\omega_2=1/\sqrt{L(C_1+C_2)}$, $U_{m2}=\sqrt{Z_2 i_L(t_7)^2+(nU_2-U_1)^2}$, $\tan\alpha_2=nU_2/(Z_2 i_L(t_7))$, $Z_2=\sqrt{L/(C_1+C_2)}$.

The resonant commutation in each dead-band of modes II, III, IV can also be analyzed in the same way.

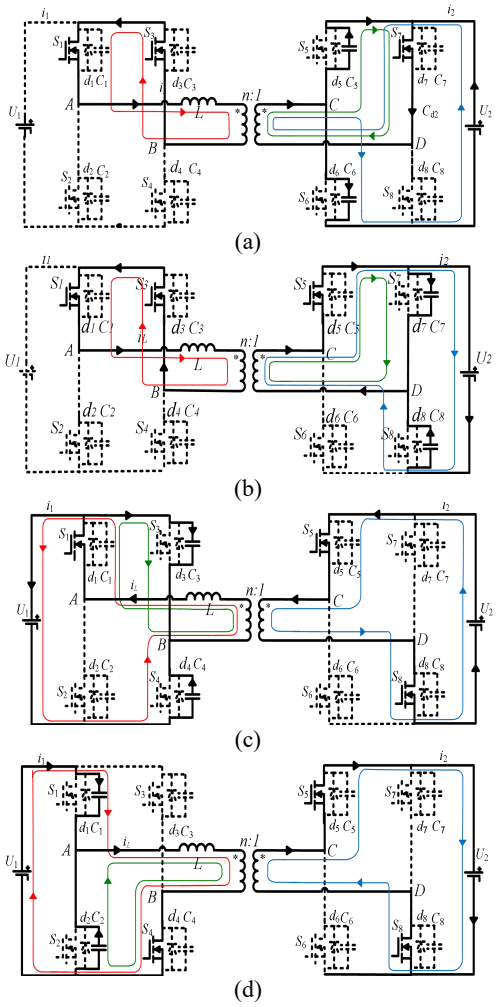

Fig. 3. Resonant commutation circuit of mode I. (a) Dead-band of [t_1, t_2]. (b) Dead-band of [t_3, t_4]. (c) Dead-band of [t_5, t_6]. (d) Dead-band of [t_7, $T_s/2$].

To achieve ZVS when the switch is turned on, it is necessary to ensure that the energy storage of the inductor in the dead-band is sufficient to complete the resonant charging and discharging process of the parallel capacitors, and then turn on the anti-parallel diode of the commutated switch. Operation mode I is also analyzed in the following as an example.

For S_1 and S_2, the inductor current in the dead-band [t_7, $T_s/2$] is required to be greater than zero, that is, $i_L(T_s/2)\geq 0$. and the voltage of C_2 should satisfy $U_{m2}\geq nU_2$ according to its voltage expression in the (18). The ZVS constraint is expressed as

$$(1-k)D_1+2kD_3\geq\max\left[2kDT,4f_s\sqrt{L\left(C_1+C_2\right)\left|2k-1\right|}\right] \tag{19}$$

For S_3 and S_4, the inductor current in [t_5, t_6] is required to be less than zero, that is, $i_L(t_6)\leq 0$, and the voltage of C_4 should satisfy $U_{m4}\geq U_1\text{-}nU_2$ according to its voltage expression in the (18). The ZVS constraint is derived as

$$(k-1)D_1+2kD_3\leq\min\left[(2k-2)DT,-4f_s\sqrt{L\left(C_3+C_4\right)\left|2k-1\right|}\right] \tag{20}$$

For S_5 and S_6, the inductor current in [t_1, t_2] is required to be greater than zero, that is, $i_L(t_1)=i_L(t_2)\geq 0$, and the voltage of C_5 can resonate to zero based on its voltage expression in the (17). This constraint is obtained as

$$-D_1+kD_2\geq 0 \tag{21}$$

For S_7 and S_8, the inductor current in [t_3, t_4] is required to be greater than zero, that is, $i_L(t_4)\geq 0$, and the voltage of C_8 should satisfy $U_{m8}\geq U_2$ according to its voltage expression in the (18). The ZVS constraint is derived as

$$-D_1+kD_2\geq\max\left[2kDT,4f_s\frac{k}{n}\sqrt{L\left(C_7+C_8\right)}\right] \tag{22}$$

Similarly, the ZVS constrains of modes II, III, and IV are as follows:

1) Operation mode II:

$$\begin{cases} (1-k)D_1+2kD_3\geq\max\left(2kDT,4f_s\sqrt{L\left(C_1+C_2\right)\left|2k-1\right|}\right) \\ D_1=kD_2 \\ (k-1)D_2+2D_3\geq 0 \end{cases} \tag{23}$$

2) Operation mode III:

$$\begin{cases} D_1=kD_2 \\ D_1+kD_2\geq\max\left(2kDT,4kf_s\sqrt{LC}/n\right) \end{cases} \tag{24}$$

3) Operation mode IV:

$$\begin{cases} (1-k)D_1+2kD_3\geq\max\left[\begin{matrix}2kDT,\\ 4f_s\sqrt{L\left(C_1+C_2\right)\left|2k-1\right|}\end{matrix}\right] \\ (k+1)D_1+2kD_3\geq\max\left[\begin{matrix}(2k+2)DT+2k,\\ 2k+4f_s\sqrt{L\left(C_3+C_4\right)}\end{matrix}\right] \\ (k+1)D_2+2D_3-2\geq 0 \\ (k-1)D_2+2D_3\geq 0 \end{cases} \tag{25}$$

In operation modes II and III, S_3, S_4, S_5, and S_6 are turned on with critical soft-switching, which refers to as the zero inductor current commutation in the dead-band. Essentially, the energy stored in the inductor cannot complete the charging and discharging of the equivalent output capacitors of the switches, and it is difficult to obtain ZVS during the commutation. Let k = 0.6, substitute the converter parameters in Section VII into (19)-(22), (23), (24) and (25), and combined with the mode constraints in (1)-(4). The operating areas of the ZVS are

This article has been accepted for publication in a future issue of this journal, but has not been fully edited. Content may change prior to final publication. Citation information: DOI 10.1109/JESTPE.2021.3135380, IEEE Journal of Emerging and Selected Topics in Power Electronics

shown in Fig. 4. The soft switching area is a small region of the entire operating area in modes I and IV, while it is only a plane in modes II and III due to the existence of equation constraints.

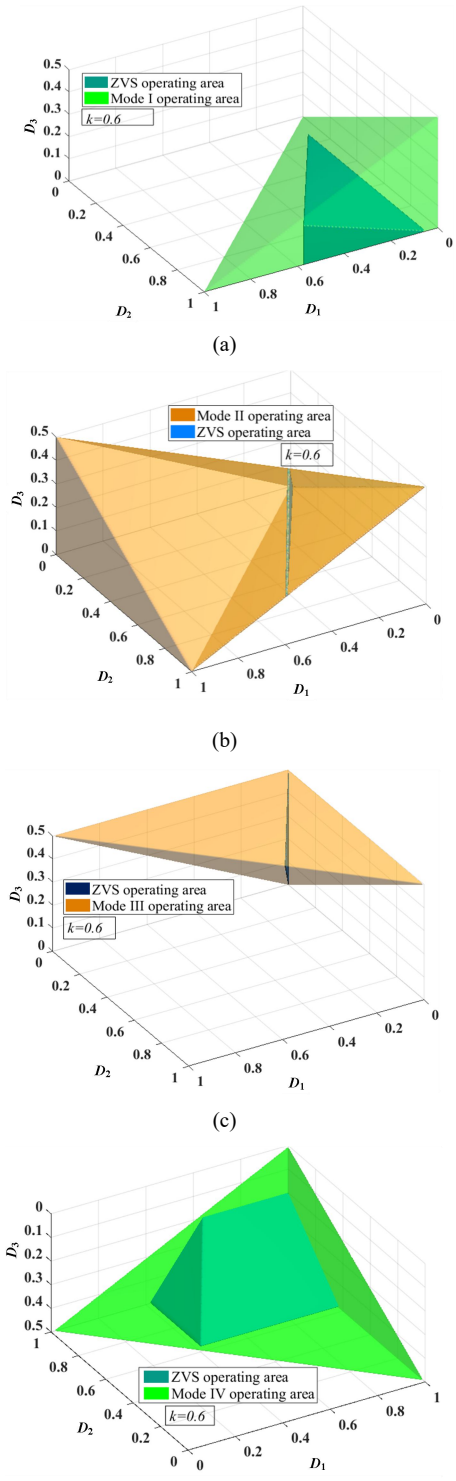

Fig. 4. ZVS operating areas of the DAB converter with TPS control. (a) Mode I. (b) Mode II. (c) Mode III. (d) Mode IV.

IV. Loss Analysis

Semiconductor losses include conduction and switching losses. In operation modes II and III, S_3, S_4, S_5, and S_6 are turned on with critical soft switches, which causes energy losses in the equivalent parallel capacitor. The energy losses are only related to the parasitic capacitor and its voltage difference. In addition, the converter can achieve ZVS at other times, and the switching loss can be ignored.

The conduction losses are caused by the switches and their anti-parallel diodes. Since the anti-parallel diodes only conduct in the dead-band, the switch conduction loss is considered. To simplify the analysis, it is assumed that the on-resistance of the switches at the primary H-bridge is R_{CEL} and the secondary H-bridge is R_{CER}. For the switch conduction loss P_{cons}, the influences of commutation in the dead-band are ignored, which is calculated as

$$P_{cons} = 2\left(R_{CEL} + n^2 R_{CER}\right) i_{Lrms}^2 \tag{26}$$

In addition to the losses of semiconductor devices, the operating losses also come from magnetic devices, including inductor and transformer. To simplify the analysis, the skin effect of high-frequency currents is ignored. Let the resistance of the inductor coil be R_L and the equivalent resistance of the transformer coil to the primary side be R_{tr}, then the copper loss of the magnetic device is derived as

$$P_{cu} = \left(R_L + R_{tr}\right) i_{Lrms}^2 \tag{27}$$

Core loss is related to core material and excitation. To simplify the analysis, it is assumed that the core losses in the magnetic devices are the same caused by sinusoidal and non-sinusoidal excitation with the same RMS. At a given frequency, the core losses of the transformer and inductor are calculated as

$$P_{fe} = K_{fe}\left(\Delta B\right)^{\beta} A_e L_e = K_{fe}\left(\frac{\sqrt{2}u_0 u_e N}{L_e}\right)^{\beta} V_e i_{Lrms}{}^{\beta} \tag{28}$$

where K_{fe} is the iron loss coefficient of the magnetic core, which increases rapidly with excitation frequency f_s. L_e is the effective magnetic path length, V_e is the effective core volume, u_0 is the vacuum permeability and u_e is the relative permeability, N is the number of turns of the coil, β is the Stan-Metz coefficient and i_{rms} is the RMS of the excitation current.

In summary, the operating losses P_{Loss} of the converter is obtained as

$$\overline{P_{Loss}} = \frac{P_{cons} + P_{cu} + P_{fe}}{P_{base}} \tag{29}$$

According to the above analysis, the operating loss is a function of the RMS of the inductor current.

V. Optimized Operation

In this section, the peak and RMS of the inductor current, the backflow power and the operating losses of the converter will be taken as the optimization objectives in each mode, and D_1, D_2, and D_3 defined in TPS are used as the decision variables. The operating mode and soft-switching constraints are used as the limit of the operating area, and the desired transmission power is added as an equality constraint. For brevity, the four

This article has been accepted for publication in a future issue of this journal, but has not been fully edited. Content may change prior to final publication. Citation information: DOI 10.1109/JESTPE.2021.3135380, IEEE Journal of Emerging and Selected Topics in Power Electronics

single-objective optimization problems with constraints in each mode are formulated as

$$\begin{cases} \text{Minimize}\left[\overline{i_p},\ \left(\overline{Q},\ \overline{i_{Lrms}},\ \overline{P_{loss}}\right)\right] \text{ in mode I (II, III and IV)} \\ s.t.\begin{cases} \text{The mode constraints in (1) ((2), (3) and (4))} \\ \text{The ZVS constraints in (18)-(21) ((22), (23) and (24))} \\ \text{The power constraints in (6) ((12), (14) and (16))} \end{cases} \end{cases} \tag{30}$$

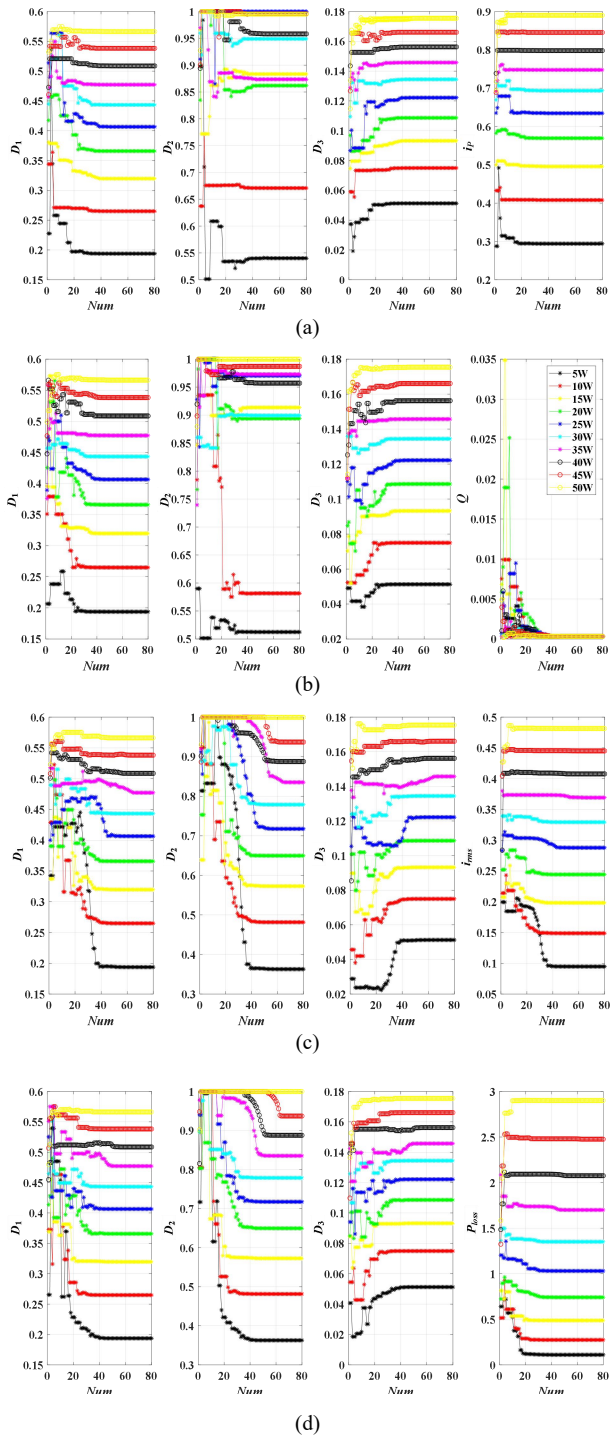

Fig. 5. Global optimal solution evolution curves for different objectives in mode I. (a) Peak current optimization. (b) Backflow power optimization. (c) RMS of current optimization. (d) Operating losses optimization.

The optimization problems are solved numerically using the particle swarm optimization (PSO) algorithm, and the converter parameters are designed in Section VII. For the PSO algorithm, $X_i = (x_{i1}, x_{i2}, \ldots, x_{in})$ is the current position of the i-th particle, and $V_i = (v_{i1}, v_{i2}, \ldots, v_{in})$ is the current velocity. $pbest_i = (pbest_1, pbest_2, \ldots, pbest_n)$ is the best position that the i-th particle has experienced, and $gbest = (gbest_1, gbest_2, \ldots, gbest_n)$ is the best position that all of the particles have experienced. The velocity and position of each particle are updated by

$$\begin{cases} v_{ij}(m+1) = \omega v_{ij}(m) + c_1 r_1\left(pbest_{ij}(m) - x_{ij}(m)\right) \\ \qquad\qquad + c_2 r_2\left(gbest_{ij}(m) - x_{ij}(m)\right) \\ x_{ij}(m+1) = x_{ij}(m) + v_{ij}(m+1) \end{cases} \tag{31}$$

where j denotes the j-th dimension in the n-dimensional space, m denotes the iteration of the particle swarm to the m-th generation, ω is the particle inertia, c_1 is the cognitive acceleration constant, c_2 is the social acceleration constant, and r_1 and r_2 are random numbers between 0 and 1. In the early stages of the iterations, the algorithm needs to have a strong global search capability to prevent prematurity. In the late stages of the iterations, a more detailed search is needed to speed up the convergence. Thus, the time-varying acceleration coefficient and inertia weight factor are adopted.

Take the process of the algorithm searching for the optimal solution in mode 1 as an example, Fig. 5 shows the evolution curves of the global optimal solution, where *Num* represents the generation of particles, and the legend in Fig. 5(b) can be applied to all curves. For mode I, certain backflow power is generated for S_3 and S_4 to achieve ZVS. This part of the energy is related to the hardware parameters and input and output voltages and has nothing to do with the transmitted power, so it will have the same minimized backflow power at different powers as shown in Fig. 5(b). For the same power, the optimal solutions (D_1, D_2, D_3) obtained by optimization of RMS current and operating losses are almost the same, and the variables (D_1, D_3) in the optimal solutions obtained by the optimizations of backflow power and peak current are consistent with those in the optimizations of RMS current and operating losses. Because the transmission power, current peak and backflow power are functions of D_1 and D_3, D_2 can be any value in the optimizations of backflow power and peak current as long as the constraints are met. These characteristics can be reflected by the convergences of the global optimal solution in Fig. 5. Thus, for mode I, duo to the calculation of operating losses is too complicated, the RMS of the inductor current can be used as the minimum objective, and the other indicators can be minimize simultaneously.

For operation modes II and III, there is no backflow power. For a certain transmission power, similarly, the optimal solutions (D_1, D_2, D_3) obtained by optimizing these four indicators in mode II are the same. Therefore, the current peak and operating losses can also be minimized simultaneously in operating mode II by using the RMS of the inductor current as the optimization objective. For mode III, the transmission power and current peak are functions of D_1 and D_2, D_3 can be any value as long as the constraints are met in peak current optimization. But the optimal variables (D_1, D_2) obtained by the

This article has been accepted for publication in a future issue of this journal, but has not been fully edited. Content may change prior to final publication. Citation information: DOI 10.1109/JESTPE.2021.3135380, IEEE Journal of Emerging and Selected Topics in Power Electronics

peak current optimization are consistent with those in the optimizations of RMS current and operating losses. Similarly, the strategy of taking the RMS of the inductor current as the optimization objective to minimize other goals simultaneously can also be adopted in mode III.

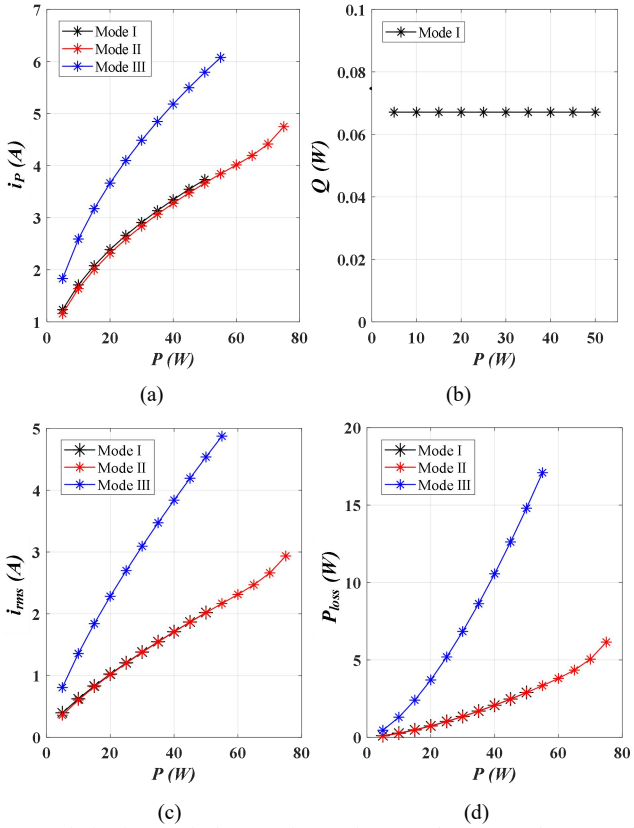

Fig. 6. Optimization results in operation mode I, II and III. (a) Peak current. (b) Backflow power. (c) RMS of current. (d) Operating losses.

For operation mode IV, the corresponding optimal solutions (D_1, D_2, D_3) obtained by different optimizing objectives are not the same, except for the optimal solutions obtained by the optimizations of RMS current and operating losses. The commonality of different optimizations in modes I, II, and III no longer exists in mode IV. For different transmission power, D_2 is equal to 1 in all optimal solutions, which indicates that the optimal operations of the DAB converter are always obtained under EPS control in mode IV. For all operating modes, duo to the global optimal solutions obtained by the optimizations of RMS current and operating losses are almost the same, the operating losses optimization will not be separately introduced in the following analysis.

As shown in Fig. 6, the converter can operate at light load in modes I, II, and III. When the transmission power is the same, the operating characteristics of the mode III converter are far worse than those of modes I and II. As the transmission power increases, this gap becomes more and more obvious. Therefore, mode III should be avoided at light load conditions. The optimized operating characteristics of modes I and II are close, and the current peak in mode I is slightly larger than that in mode II. The power transmission range of mode I is much lower than that of mode II.

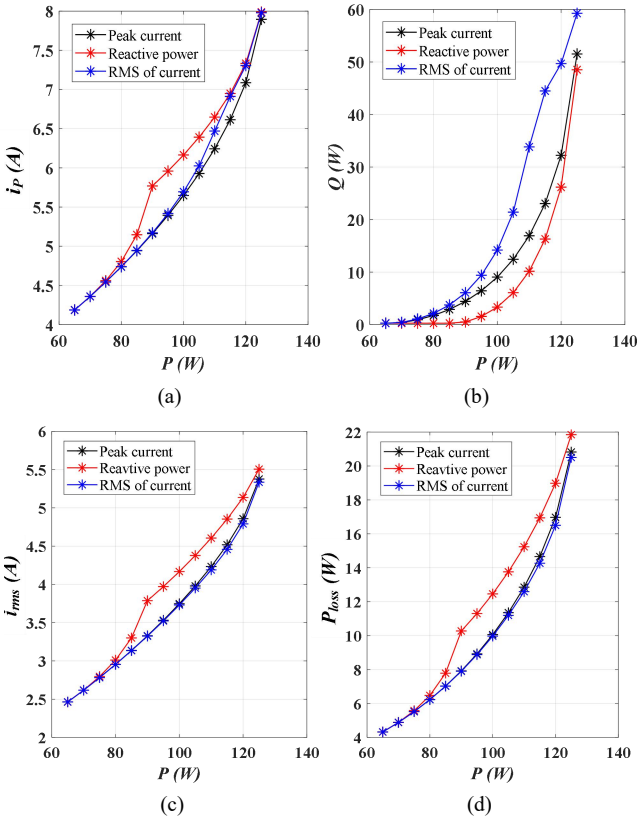

Fig. 7. Optimization results with different objectives in mode IV. (a) Peak current. (b) Backflow power. (c) RMS of current. (d) Operating losses.

As shown in Fig. 7, the legend shows the corresponding optimization objective, and the optimization objectives in the operation mode IV cannot be minimized at the same time. The current peaks corresponding to the optimal solutions obtained by the peak and RMS of inductor current optimization are close, but the backflow power caused by the RMS optimization is much larger than that in the other two optimization results. For the RMS of current and operating losses, the performance obtained by the RMS of current optimization is the best, but the results obtained by peak current optimization are very close to them, and the backflow power optimization is the worst.

VI. Experiment Results

To validate the analysis and the optimization results, experimental tests are performed. For the experimental prototype, the input voltage is 50 V, and the output is connected to a battery with a rated voltage of 12 V. IRF540NPBF MOSFETs from Infineon Technologies are used, and the dead-band is set to 0.5 us. Other parameters of the prototype are shown in Table II.

TABLE II
Parameters of Prototype

Parameter	Value	Parameter	Value
U_1	50 V	U_2	10.8-14.4 V
f_s	20 KHz	DT	0.5 us
R_{CEL} (R_{CER})	44 mΩ	C_L/C_R	1.3/8.2 nF

This article has been accepted for publication in a future issue of this journal, but has not been fully edited. Content may change prior to final publication. Citation information: DOI 10.1109/JESTPE.2021.3135380, IEEE Journal of Emerging and Selected Topics in Power Electronics

TABLE III
PARAMETERS OF TRANSFORMER

Parameter	Value	Parameter	Value
Turns ratio	2.5:1	u_e	119
A_e	170 mm^2	L_e	99 mm
K_{fe}	5.915	L_k	2.3uH
R_p /R_s	15.53/3.12 mΩ	β	2.479

TABLE IV
PARAMETERS OF INDUCTOR

Parameter	Value	Parameter	Value
L_L	72.2 uH	u_e	60
A_e	229 mm^2	L_e	125 mm
K_{fe}	1.24	R_L	8.9 mΩ
N	23	β	2.01

For the high-frequency transformer, there is a large margin for the power level of the selected core, which is TDK ferrite core ER42/15. The measured parameters of the transformer are shown in Table III. Where R_p is the resistance of the primary coil and R_s the secondary coil. L_k is a leakage inductor. The inductor adopts the iron silicon aluminum powder core. The measured parameters of the inductor are shown in Table IV.

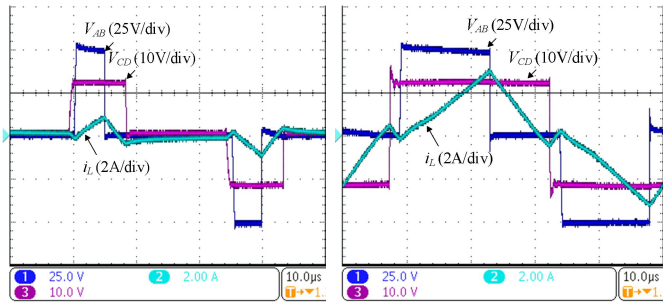

(a) (b)

Fig. 8. Operation waveforms of mode I. (a) P = 5 W. (b) P = 50 W.

The operating waveforms of mode I at steady state are shown in Fig. 8. The rising edge of V_{AB} from 0 to U_1 lags the rising edge of V_{CD} from 0 to U_2, which causes the inductor current to fall below zero. For different powers, the lagges time is the same, which leads to the same drop in current. According to the theoretical analysis, this part of the current is the condition for S_3 and S_4 to complete the resonant commutation to achieve ZVS, and it is also the cause of backflow power, which has nothing to do with the transmission power. The experimental results are consistent with the theoretical analysis. Based on Fig. 8, the constraint of the ZVS on the direction and amplitude of the inductor current increases the RMS of the current, which degrades the operating efficiency. However, as the power increases, the resulting RMS increase becomes smaller and smaller.

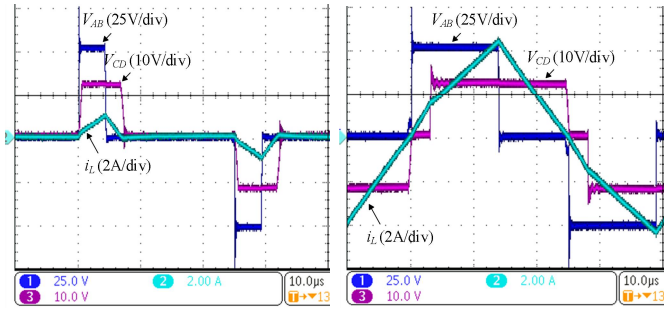

(a) (b)

Fig. 9. Operation waveforms of mode II. (a) P = 5 W. (b) P = 75 W.

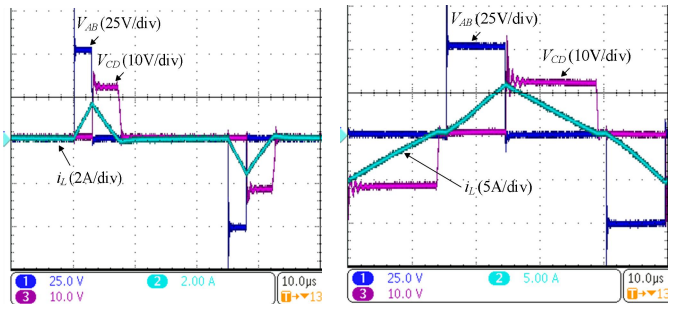

(a) (b)

Fig. 10. Operation waveforms of mode III. (a) P = 5 W. (b) P = 55 W.

Figs. 9 and 10 show the experimental waveforms of modes II and III respectively. There are critical soft-switching state for certain switching devices, that is, the inductor current remains at zero during commutation, which can be demonstrated by the experiments. For commutation in other dead-bands, the direction of the inductor current can meet the soft switching constraints in the corresponding operation mode according to these waveforms. Based on Fig. 9, for mode II, the rising edge of V_{AB} from 0 to U_1 does not lead to the rising edge of V_{CD} from zero to U_2, which avoids the generation of backflow power and avoids the increase in the RMS of the current. It is beneficial to improve the converter efficiency. For mode III, the peak current is significantly larger, and as the power increases, this trend becomes more obvious according to Fig. 10.

Fig. 11 shows the waveforms of the optimized operation obtained by different objectives in mode IV, where V_{CD} is a square wave, i.e., D_2 =1. According to Figs. 11(d), (e), and (f), the rising edge of V_{AB} from 0 to U_1 lags the rising edge of V_{CD} from -U_2 to U_2, and the inductor current crosses the zero between them, which ensures that the inductor current is less than zero when S_4 is turned on and greater than zero when S_5, S_8 is turned on. As the transmission power decreases, the two rising edges described above gradually approach the critical state shown in Figs. 11(a), (b) and (c), which is close to the minimum transmission power of mode IV. It can be seen from the current waveforms in Fig. 11 that the current direction satisfies the zero-voltage turn-on condition of all switches, but in this mode, the inductor current that causes backflow power increases significantly. By comparison, the optimized operating waveforms obtained by different optimization objectives are similar, which indicates that the converter's performance is close in this mode.

This article has been accepted for publication in a future issue of this journal, but has not been fully edited. Content may change prior to final publication. Citation information: DOI 10.1109/JESTPE.2021.3135380, IEEE Journal of Emerging and Selected Topics in Power Electronics

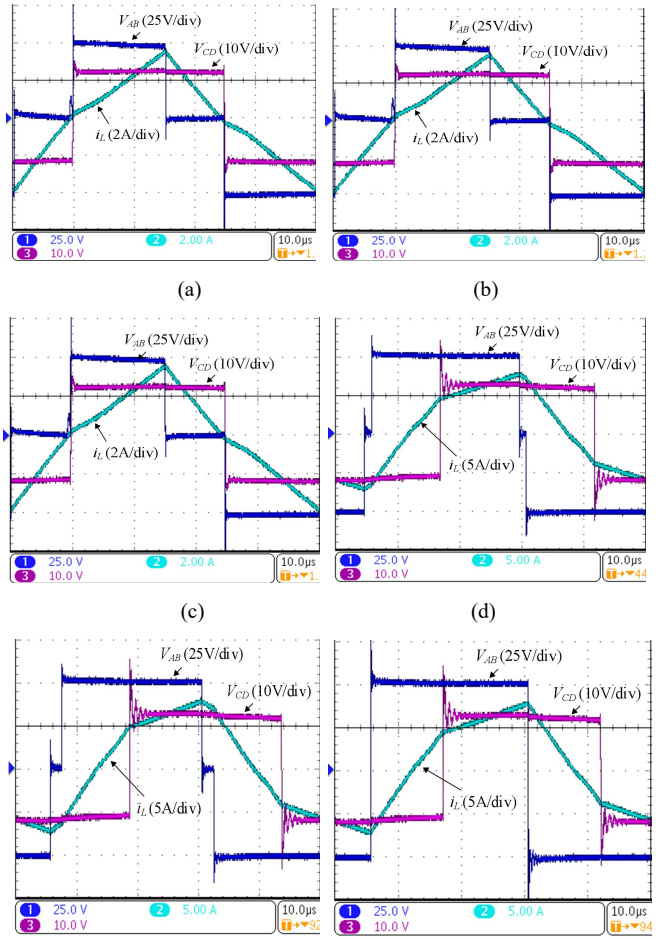

Fig. 11 Operation waveforms with different objectives in mode IV. (a) Peak current optimization when P = 65 W. (b) Backflow power optimization when P = 65 W. (c) RMS of current optimization when P = 65 W. (d) Peak current optimization when P = 125 W. (e) Backflow power optimization when P = 125 W. (f) RMS of current optimization when P = 125 W.

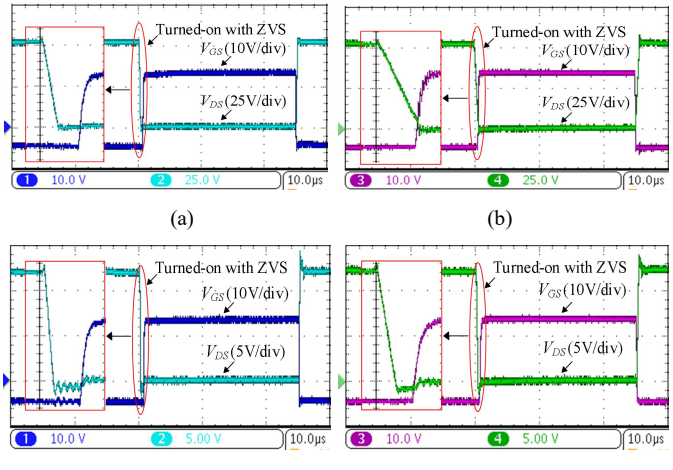

Fig. 12 Gate-source and drain-source voltages of switches in mode I when P = 5 W. (a) S_1. (b) S_3. (c) S_5. (d) S_7.

At light load, the converter can operate in modes I, II, and III, and at heavy load only in mode IV. When the transmission powers are the same, the operating characteristics of mode III are far inferior to other modes. Therefore, for ZVS characteristics, only operation modes I, II, and IV are analyzed. Due to the symmetry of the converter operation, only the gate-source and drain-source voltages of the upper switch on each bridge are presented.

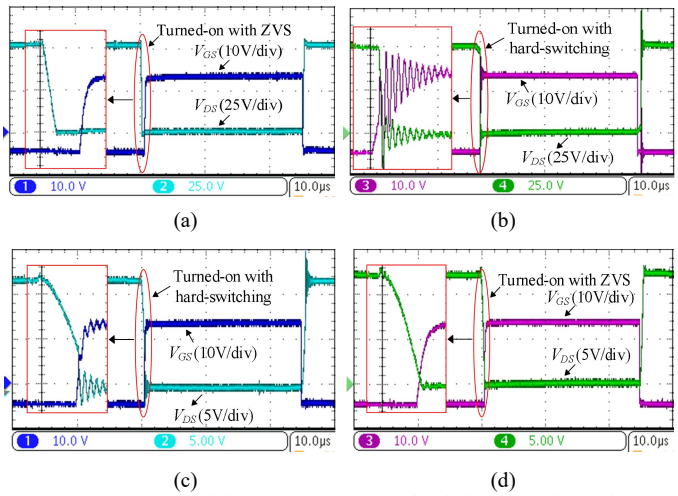

Fig. 13 Gate-source and drain-source voltage of switches in mode II when P = 5 W. (a) S_1. (b) S_3. (c) S_5. (d) S_7.

For mode I, theoretical analysis and current waveforms demonstrate that all switches have excellent soft-switching characteristics. As shown in Fig. 12, when the gate-source voltages of the switches start to rise, the drain-source voltages have dropped to zero, so the theoretical analysis is well proved again. For mode II, in theoretical analysis, S_1, S_2, S_7, S_8 are turned on with ZVS, and S_3, S_4, S_5, S_6 are critical soft switches. Similarly, the corresponding voltage waveforms of mode II when the switches are turned on, are shown in Fig. 13. Before the switches S_1 and S_7 are turned on, the drain-source voltages have dropped to zero, as shown in Figs. 13(a) and (d), and the ZVS characteristics are satisfactory. By contrast, for the switches S_3 and S_5, based on Fig. 9, the inductor currents are zero when they are turned on, which cannot transfer the energy stored in their parasitic capacitors and can not turn on the anti-parallel diodes, which is called the critical soft switching state. According to the voltage waveforms in Figs. 13(b) and (c), this is hard switching. For mode IV, the experimental results are consistent with the theoretical analysis, and all switches have ZVS turn-on characteristics, as demonstrated in Fig. 14.

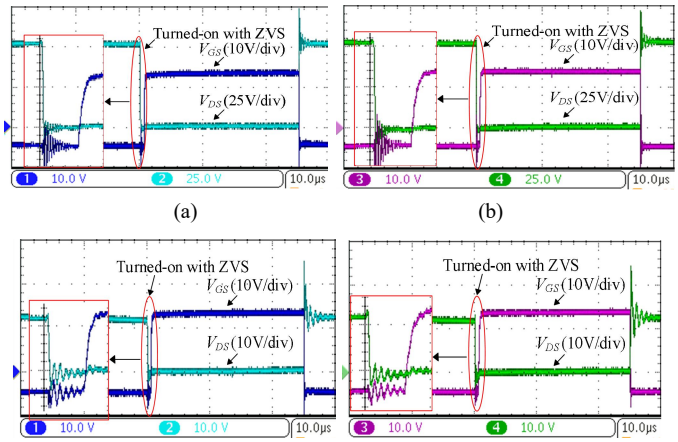

Fig. 14 Gate-source and drain-source voltage of switches in mode IV when P = 125 W. (a) S_1. (b) S_3. (c) S_5. (d) S_7.

This article has been accepted for publication in a future issue of this journal, but has not been fully edited. Content may change prior to final publication. Citation information: DOI 10.1109/JESTPE.2021.3135380, IEEE Journal of Emerging and Selected Topics in Power Electronics

Fig. 15 shows the efficiency of the converter with different optimization objectives measured in the experiments. At light load, the efficiency of mode II is slightly higher than that of mode I. Mode III has the worst operating characteristics, which leads to its lower operating efficiency. At light load, as the transmission power increases, the converter efficiency gradually increases. At heavy load, the converter can only operate in mode IV, the backflow power optimization has the lowest efficiency, and the efficiency corresponding to RMS of inductor current optimization is slightly higher than one peak current optimization. At heavy load, as the transmission power increases, the converter efficiency decreases. The operating efficiency of mode IV is higher than that of mode II for the same transmission power, which is close to the maximum efficiency of the converter.

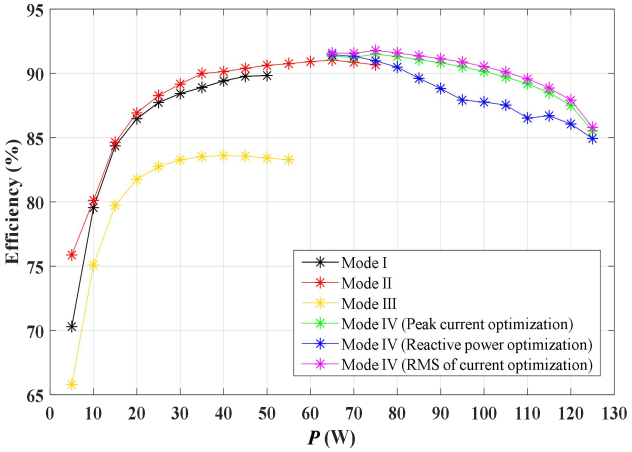

Fig. 15. Efficiency of the DAB converter.

At light load, comparing the optimization results of different objectives with different operating modes, the converter should avoid operate in mode III, and the performances of modes I and II are close. All switches in mode I have excellent ZVS characteristics, but a small amount of backflow power will be induced. In mode II, only half of the switches are turned on with ZVS, but there is no backflow power, and the operating efficiency is slightly higher than that of mode I. For modes I, II, and III, the RMS of the inductor current can be used as the optimization objective because it can also minimize other optimization objectives simultaneously. At heavy load, the converter can only operate in mode IV, and the results of RMS and peak current optimizations are close. The operating characteristics of the converter with backflow power optimization are worse. Thus, backflow power optimization should be avoided at heavy loading conditions.

VII. Conclusion

This paper presents an in-depth comparative optimization analysis for DAB converters with the phase-shift control in the ZVS operating areas. As an integrated research of modulation and optimization, the major efforts and contributions include: 1) Since the other modulations are only special cases of it, the TPS control is adopted in the paper, which covers all modulation characteristics of phase-shift control. 2) The operating characteristics and soft-switching areas of the converter with TPS control are systematically derived, which is applicable to related researches. 3) The optimization objectives analyzed in the paper are extensive and representative. At light loads, on the basis of the comparative analysis, the operating mode III is not desirable due to its harsh characteristics. 4) The commonality of the optimization results with different objectives in modes I, II and III are revealed, and the RMS of the inductor current can be used as the optimization objective in these modes because it can also minimize other objectives simultaneously. 5) The operating performances of the converter obtained by different objectives are comparatively analyzed in mode IV. It is not advisable for the backflow power optimization, while the operating characteristics of the converter obtained by the RMS and peak value of current optimization are close, which can provide inspiration for the selection of optimization objectives for heavy load conditions.

References

[1] N. Hou, and Y. Li, "Overview and Comparison of Modulation and Control Strategies for a Nonresonant Single-Phase Dual-Active-Bridge DC–DC Converter," *IEEE Trans. Power Electron.*, vol. 35, no. 3, pp. 3148-3172, Mar. 2020.

[2] G. Xu, D. Sha, Y. Xu, and X. Liao, "Dual-Transformer-Based DAB Converter With Wide ZVS Range for Wide Voltage Conversion Gain Application," *IEEE Trans. Ind. Electron.*, vol. 65, no. 4, pp. 3306-3316, Apr. 2018.

[3] Y. Shi, R. Li, Y. Xue, and H. Li, "Optimized Operation of Current-Fed Dual Active Bridge DC–DC Converter for PV Applications," *IEEE Trans. Ind. Electron.*, vol. 62, no. 11, pp. 6986-6995, Nov. 2015.

[4] Y. Yan, H. Bai, A. Foote, and W. Wang, "Securing Full-Power-Range Zero-Voltage Switching in Both Steady-State and Transient Operations for a Dual-Active-Bridge-Based Bidirectional Electric Vehicle Charger," *IEEE Trans. Power Electron.*, vol. 35, no. 7, pp. 7506-7519, Jul. 2020.

[5] H. Shi, H. Wen, J. Chen, Y. Hu, L. Jiang, and G. Chen, "Minimum-Backflow-Power Scheme of DAB-Based Solid-State Transformer With Extended-Phase-Shift Control," *IEEE Trans. Ind. Appl.*, vol. 54, no. 4, pp. 3483-3496, Jul.-Aug. 2018.

[6] T. M. Parreiras, A. P. Machado, F. V. Amaral, G. C. Lobato, J. A. S. Brito, and B. C. Filho, "Forward Dual-Active-Bridge Solid-State Transformer for a SiC-Based *Cascaded* Multilevel Converter Cell in Solar Applications," *IEEE Trans. Ind. Appl.*, vol. 54, no. 6, pp. 6353-6363, Nov.-Dec. 2018.

[7] Y. Xuan, X. Yang, W. Chen, T. Liu, and X. Hao, "A Novel NPC Dual-Active-Bridge Converter With Blocking Capacitor for Energy Storage System," *IEEE Trans. Power Electron.*, vol. 34, no. 11, pp. 10635-10649, Nov. 2019.

[8] A. K. Bhattacharjee, and I. Batarseh, "Optimum Hybrid Modulation for Improvement of Efficiency Over Wide Operating Range for Triple-Phase-Shift Dual-Active-Bridge Converter," *IEEE Trans. Power Electron*, vol. 35, no. 5, pp. 4804-4818, May 2020.

[9] B. Zhao, Q. Song, J. Li, and W. Liu, "A Modular Multilevel DC-Link Front-to-Front DC Solid-State Transformer Based on High-Frequency Dual Active Phase Shift for HVDC Grid Integration," *IEEE Trans. Ind. Electron.s*, vol. 64, no. 11, pp. 8919-8927, Nov. 2017.

[10] N. Hou, W. Song, Y. Zhu, X. Sun and W. Li, "Dynamic and static performance optimization of dual active bridge DC-DC converters," *J. Mod. Power Syst. Clean Energy*, vol. 6, no. 3, pp. 607-618, May 2018.

[11] M. Yang, "PWM Plus Phase-Shift Control for Dual Active Full-Bridge DC-DC Converter" M.S. thesis, Dept. Electrical. Eng., Nanjing Univ of Aeronautics and Astronautics., Nanjing, China, 2013.

[12] P. Liu, C. Chen, S. Duan, and W. Zhu, "Dual Phase-Shifted Modulation Strategy for the Three-Level Dual Active Bridge DC–DC Converter," *IEEE Trans. Ind. Electron.*, vol. 64, no. 10, pp. 7819-7830, Oct. 2017.

[13] H. Wen, and B. Su, "Reactive power and soft-switching capability analysis of dual-active-bridge dc-dc converters with dual-phase-shift control," *J. Power Electron.*, vol. 15, no. 1, pp. 18-30, 2015.

[14] B. Zhao, Q. Yu, and W. Sun, "Extended-Phase-Shift Control of Isolated Bidirectional DC–DC Converter for Power Distribution in Microgrid," *IEEE Trans. Power Electron.*, vol. 27, no. 11, pp. 4667-4680, Nov. 2012.

[15] L. Jiang, Y. Sun, M. Su, H. Wang, and H. Dan, "Optimized operation of dual-active-bridge dc-dc converters in the soft-switching area with

triple-phase-shift control at light loads," *J. Power Electron.*, vol. 18, no. 1, pp. 45-55, 2018.
[16] A. Tong, L. Hang, G. Li, X. Jiang, and S. Gao, "Modeling and analysis of a dual-active-bridge-isolated bidirectional dc/dc converter to minimize RMS current with whole operating range," *IEEE Trans. Power Electron.*, vol. 33, no. 6, pp. 5302–5316, Jun. 2018.
[17] N. Hou, W. Song, Y. Li, Y. Zhu, and Y. Zhu, "A Comprehensive Optimization Control of Dual-Active-Bridge DC–DC Converters Based on Unified-Phase-Shift and Power-Balancing Scheme," *IEEE Trans. Power Electron.*, vol. 34, no. 1, pp. 826-839, Jan. 2019.
[18] F. Wu, F. Feng, and H. B. Gooi, "Cooperative Triple-Phase-Shift Control for Isolated DAB DC–DC Converter to Improve Current Characteristics," *IEEE Trans. Ind. Electron.*, vol. 66, no. 9, pp. 7022-7031, Sep. 2019.
[19] Z. Li, Y.Wang, L. Shi, J. Huang, and W. Lei, "Optimized modulation strategy for three-phase dual-active-bridge DC-DC converters to minimize RMS inductor current in the whole load range," 2016 IEEE 8th International Power Electronics and Motion Control Conference (IPEMC-ECCE Asia), Hefei, 2016, pp. 2787-2791.
[20] D. Sha, J. Zhang, and K. Liu, "Leakage Inductor Current Peak Optimization for Dual-Transformer Current-Fed Dual Active Bridge DC–DC Converter With Wide Input and Output Voltage Range," *IEEE Trans. Power Electron.*, vol. 35, no. 6, pp. 6012-6024, Jun. 2020.
[21] O. M. Hebala, A. A. Aboushady, K. H. Ahmed, and I. Abdelsalam, "Generic Closed-Loop Controller for Power Regulation in Dual Active Bridge DC–DC Converter With Current Stress Minimization," *IEEE Trans. Ind. Electron.*, vol. 66, no. 6, pp. 4468-4478, Jun. 2019.
[22] H. Shi et al., "Minimum-Backflow-Power Scheme of DAB-Based Solid-State Transformer With Extended-Phase-Shift Control," in IEEE Transactions on Industry Applications, vol. 54, no. 4, pp. 3483-3496, July-Aug. 2018.
[23] H. Shi, H. Wen, J. Chen, Y. Hu, L. Jiang, and G. Chen, "Minimum-Reactive-Power Scheme of Dual-Active-Bridge DC–DC Converter With Three-Level Modulated Phase-Shift Control," *IEEE Trans. Ind. Appl.*, vol. 53, no. 6, pp. 5573-5586, Nov.-Dec. 2017.
[24] S. Shao, M. Jiang, W. Ye, Y. Li, J. Zhang, and K. Sheng, "Optimal Phase-Shift Control to Minimize Reactive Power for a Dual Active Bridge DC–DC Converter," *IEEE Trans. Power Electron.*, vol. 34, no. 10, pp. 10193-10205, Oct. 2019.
[25] F. Krismer and J. W. Kolar, "Closed Form Solution for Minimum Conduction Loss Modulation of DAB Converters," *IEEE Trans. Power Electron*, vol. 27, no. 1, pp. 174-188, Jan. 2012.
[26] B. Zhao, Q. Song and W. Liu, "Efficiency Characterization and Optimization of Isolated Bidirectional DC – DC Converter Based on Dual-Phase-Shift Control for DC Distribution Application," *IEEE Trans. Power Electron*, vol. 28, no. 4, pp. 1711-1727, April. 2013.

Li Jiang (S'18) was born in Hunan, China, in 1991. He received B.S. degree from the Hunan University of Technology, Zhuzhou, China, in 2015, and the M.S. degree from Central South University, Changsha, China, in 2018, both in Control Science and Engineering. He is currently working toward the Ph.D. degree in electrical engineering at Hunan University, Changsha, China. His current research interests include bidirectional DC/DC converters, Soft-switching technology, modeling and charging strategy for Li-ion battery.

Yao Sun (M'13) was born in Hunan, China, in 1981. He received his B.S., M.S. and Ph.D. degrees from the School of Information Science and Engineering, Central South University, Changsha, China, in 2004, 2007 and 2010, respectively. He is presently working as a Professor in the School of Automation, Central South University. His current research interests include matrix converters, microgrids and wind energy conversion systems.

Yong Li（S'09-M'12-SM'14) was born in Henan, China, in 1982. He received the B.Sc. and Ph.D. degrees in 2004 and 2011, respectively, from the College of Electrical and Information Engineering, Hunan University, Changsha, China. Since 2009, he worked as a Research Associate at the Institute of Energy Systems, Energy Efficiency, and Energy Economics (ie3), TUDortmund University, Dortmund, Germany, where he received the second Ph.D. degree in June 2012. After then, he was a Research Fellow with The University of Queensland, Brisbane, Australia. Since 2014, he is a Full Professor of electrical engineering with Hunan University. His current research interests include power system stability analysis and control, ac/dc energy conversion systems and equipment, analysis and control of power quality, and HVDC and FACTS technologies.

Zhongting Tang (M'21) was born in Sichuan, China, in 1990. She received her B.S. degree in Automation Control in 2012 and Ph.D. degree in Control Science and Engineering in 2020 from Central South University, Changsha, China. During 2018~2020, she studied as a guest Ph.D. student at the AAU Energy in Aalborg University, Aalborg, Denmark. Now, she is currently working as a postdoc here.

Her research focus is on the grid integration of photovoltaics, topology and modulation technology of transformerless converter and its application and reliability in Photovoltaic system.

Fulin Liu received the B.S. and M.S. degrees from the School of Automation, Central South University, Changsha, China, in 2016 and 2019, respectively, where he is currently working toward Ph.D. degree in control science and engineering. His research interests include battery management system, battery equalizers and dc/dc converters.

Yongheng Yang (SM'17) received the B.Eng. degree in Electrical Engineering and Automation from Northwestern Polytechnical University, China, in 2009 and the Ph.D. degree in Energy Technology (power electronics and drives) from Aalborg University, Denmark, in 2014.

He was a postgraduate student with Southeast University, China, from 2009 to 2011. In 2013, he spent three months as a Visiting Scholar at Texas A&M University, USA. Since 2014, he has been with the Department of Energy Technology, Aalborg University, where he became a tenured Associate Professor in 2018. In January 2021, he joined Zhejiang University, China, where he is currently a ZJU100 Professor with the Institute of Power Electronics. His research

is focused on the grid-integration of photovoltaic systems and control of power converters, in particular, the grid-forming technologies.

Dr. Yang was the Chair of the IEEE Denmark Section (2019-2020). He is an Associate Editor for several IEEE Transactions/Journals. He is a Deputy Editor of the *IET Renewable Power Generation* for Solar Photovoltaic Systems. He was the recipient of the 2018 *IET Renewable Power Generation* Premium Award and was an Outstanding Reviewer for the IEEE TRANSACTIONS ON POWER ELECTRONICS in 2018. He received the 2021 Richard M. Bass Outstanding Young Power Electronics Engineer Award from the IEEE Power Electronics Society (PELS). In addition, he has received two IEEE Best Paper Awards. He is currently the Secretary of the IEEE PELS Technical Committee on Sustainable Energy Systems and a Council Member of the China Power Supply Society.

Mei Su was born in Hunan, China, in 1967. She received her B.S. and M.S. degrees in Industrial Automation, and her Ph.D. degree in Control Science and Engineering from the School of Information Science and Engineering, Central South University, Changsha, China, in 1989, 1992 and 2005, respectively. Since 2006, she has been working as a Professor in the School of Automation, Central South University. Her current research interests include matrix converters, adjustable speed drives and wind energy conversion systems.

Yijia Cao (M'98) was born in Hunan, China, in 1969. He graduated from Xi'an Jiaotong University, Xi'an, China in 1988 and received M.Sc. degree from Huazhong University of Science and Technology (HUST), Wuhan, China in 1991 and Ph.D. from HUST in 1994. From September 1994 to April 2000, he worked as a visiting research fellow, research fellow at Loughborough University, Liverpool University and University of the WestEngland, UK. From 2000 to 2001, he was employed as a full professor of HUST, and from 2001 to 2008, he was employed as a full professor of Zhejiang University, China. He was appointed deputy dean of College of Electrical Engineering, Zhejiang University in 2005. Currently, he is a full professor and president of Changsha University of Science and Technology, Changsha, China. His research interests are power system stability control and the application of intelligent systems in power systems.